Published in final edited form as:
Neuroimage. 2014 May 15; 92: 156–168. doi:10.1016/j.neuroimage.2014.01.053.

Automated Segmentation and Shape Characterization of Volumetric Data

Vitaly L. Galinsky[a,c,*] and **Lawrence R. Frank**[a,b,**]

[a]Center for Scientific Computation in Imaging, University of California at San Diego, La Jolla, CA 92093-0854, USA

[b]Center for Functional MRI, University of California at San Diego, La Jolla, CA 92093-0677, USA

[c]Electrical and Computer Engineering Department, University of California at San Diego, La Jolla, CA 92093-0407, USA

Abstract

Characterization of complex shapes embedded within volumetric data is an important step in a wide range of applications. Standard approaches to this problem employ surface based methods that require inefficient, time consuming, and error prone steps of surface segmentation and inflation to satisfy the uniqueness or stability of subsequent surface fitting algorithms. Here we present a novel method based on a spherical wave decomposition (SWD) of the data that overcomes several of these limitations by directly analyzing the entire data volume, obviating the segmentation, inflation, and surface fitting steps, significantly reducing the computational time and eliminating topological errors while providing a more detailed quantitative description based upon a more complete theoretical framework of volumetric data. The method is demonstrated and compared to the current state-of-the-art neuroimaging methods for segmentation and characterization of volumetric magnetic resonance imaging data of the human brain.

Keywords

Spherical harmonics; spherical wave decomposition; morphometry; segmentation

1. Introduction

Characterization of complex shapes embedded within volumetric data is an important step in a wide range of applications. In neuroimaging applications, for example, quantitative descriptions of brain morphology play a critical role in the characterization of neurodegenerative disease progression. Standard approaches to this problem employ surface based methods that require an initial segmentation of a surface and often a subsequent

[*]Principal corresponding author. [**]Corresponding author vit@ucsd.edu (Vitaly L. Galinsky), lfrank@ucsd.edu (Lawrence R. Frank).

inflation of this surface to satisfy the uniqueness or stability of subsequent surface fitting algorithms. These methods are inefficient and time consuming because of the need for segmentation prior to fitting and the computationally intensive inflation process, the latter of which being also a significant source of errors due to creation of topological defects. Here we present a novel method that overcomes several of these limitations by directly analyzing the entire data volume, obviating the segmentation, inflation, and surface fitting steps, significantly reducing the computational time and eliminating topological errors while providing a more detailed quantitative description based upon a more complete theoretical framework of volumetric data. The method is based on a spherical wave decomposition (SWD) of the data and we present an application of this technique to volumetric magnetic resonance imaging (MRI) data of the human brain.

This novel 3D signature-based method produces rotationally invariant compact shape descriptors that can be efficiently computed over 3D datasets without the need for explicit preliminary surface segmentation. The approach is appropriate for compact representation, fast decomposition, and automated segmentation and morphometry analyses of volumetric magnetic resonance imaging data. The SWD representation uses a direct expansion of volumetric data in a linear combination of basis functions that include both angular (spherical harmonics) and radial (spherical Bessel functions) parts. The 3D descriptors are easily archived and facilitate statistical comparison at multiple spatial scales: low frequency information describes gross shape, while high frequency information captures more detail as well as internal structures.

Direct computation of the SWD over a full volume of data is computationally expensive, and thus we developed several fast transforms applicable both to spherical harmonics and to spherical Bessel functions that allowed a fast and robust numerical implementation of the SWD that is applicable to a wide range of geometries, independent of affine transformations, for large, noisy volumetric data sets. We demonstrate this method on a high resolution MRI data set of a normal human brain by comparing it to the current state-of-the-art methods employed in neuroimaging for segmentation of gray and white matter and shape characterization of the cortical surface.

2. Background

Continuing progress in the development of advanced non-invasive imaging methods such as MRI and CT have facilitated the acquisition of very high resolution, high contrast volumetric data that offers the possibility of non-invasive highly informative assessment of brain morphology. However, these more informative and complex data puts a greater burden on the computational methods needed to analyze them. This is particularly true of MRI data which has a wide range of contrast mechanisms by which it can produce very high contrast between complex soft tissues of different types.

In concert with these advancements in imaging technologies, advances in computational methods, particularly in volume graphics and computer vision has resulted in tremendous increase in computational methods for morphology characterization and segmentation for comparative morphometry for both basic neuroscience studies on brain anatomy and clinical

studies of disease characterization and progression in humans, and for a broad range of studies in comparative biology.

In comparative biology, geometric morphometrics has emerged as an important tool for analysis, becoming commonly used to quantify morphology, wherein landmark points are identified in photographic (2D) images and then are fit to a warped mesh that provides a common coordinate system in which different specimens can be compared (Zelditch et al., 2004). These methods allow users to define key points of known morphological interest and statistically compare morphologies based on these points. However, the current predominant methods are based on 2D digital images or on 3D surfaces and are not readily applied to volumetric 3D data, such as those acquired by MRI or CT.

Recent advances in segmentation techniques were mostly originated from fuzzy logic and supervised and non-supervised clustering (Barra and Boire, 2000; Lin et al., 2012) both in 2D (Barra and Boire, 2001; Cocuzzo et al., 2011; Pedoia and Binaghi, 2012; Razlighi et al., 2012; Suri, 2001; Zavaljevski et al., 2000) and 3D (He et al., 2011; Kiebel et al., 2000; Klauschen et al., 2009; Popuri et al., 2012; Wels et al., 2011). Unfortunately, in spite of all advances none of these methods are able to provide truly robust and automated segmentation.

The most straightforward approach to segmentation is thresholding, which involves finding an intensity value, the threshold, that distinguishes features of interest. This method is most frequently used to create a binary segmentation of an image, but it is also possible to distinguish three or more intensity classes using multithresholding (Zavaljevski et al., 2000). Thresholding works particularly well with imaging modalities such as CT data where images are often essentially binary between bone (bright) and soft tissue (very dark) and segmentation can be practically automated. Automated methods for MRI data, however, are exceedingly difficult because of adjoining regions with similar values (i.e. low contrast), partial voluming (multiple tissue types within a single voxel), image noise, and intensity inhomogeneities, all of which are common to MR images (Atkins and Mackiewich, 2000; Pham et al., 2000).

Region growing methods extract connected regions in images based on criteria that can include both intensity and edges. These methods are susceptible to noise, which can create artificial divisions between connected regions, and partial volume effects, which can merge disconnected regions. These effects can be reduced by limiting growth to topology-preserving deformations (Mangin et al., 1995), but user input is still required to select seed regions. Clustering algorithms alternate between segmenting the image and characterizing the properties of each segmented class, iterating until a stopping criterion is reached (Barra and Boire, 2000, 2002; Liang et al., 1994; Pachai et al., 2001; Popuri et al., 2012). Clustering is generally susceptible to both noise and image inhomogeneities, though robustness to intensity inhomogeneities has been demonstrated (Pham and Prince, 1999). Given a Bayesian prior model, Markov random field models can be incorporated in clustering methods to minimize susceptibility to noise (Li, 1994).

Atlas-guided approaches provide an option that may be feasible (Klein et al., 2009). In such methods, a linear or non-linear transformation is found mapping the pre-segmented atlas image to the target image. Thus the tissue classification problem is changed to a registration or deformation problem. However, to effectively use atlas-guided methods very large and detailed databases or atlases of reference objects are needed. This puts the onus of the quantitation on an accurate and reproduceable method for atlas creation.

One important and rather successful direction in brain quantifying and characterization has emerged from analyses of parameterization of surfaces for 3D shape description using spherical harmonics (SPHARM) representation (Brechbühler et al., 1995; Kazhdan et al., 2003). Shape signatures can be created using the SPHARM decomposition at several concentric spheres or just at a single surface that represents a highly convoluted geometry of the cerebral cortex. In the SPHARM method any function f is assumed to be defined on a sphere, $f(\theta, \varphi)$, and decomposed as the sum of its spherical harmonics:

$$f(\theta,\phi)=\sum_{l=0}^{\infty}\sum_{m=-l}^{l} f_{lm}\, Y_l^m\,(\theta,\phi) \quad (1)$$

with low values of l corresponding to lower frequency information. Since L_2-norms of spherical functions are not affected by rotations, a rotationallyinvariant shape signature may be given as $SH(f) = \{\|f_0(\theta, \varphi)\|, \|f_1(\theta, \varphi)\|, \ldots\}$, where the $f_l(\theta,\phi)=\sum_{m=-l}^{l} f_{lm} Y_l^m(\theta,\phi)$ are the frequency components of f. We note that an alternate signature can be calculated more quickly and directly from the coefficients, defining $SH(f) = \{A_0, A_1, \ldots\}$, where the A_l are L_2-norms of all the coefficients f_{lm} at each l: $A_l=\sum_{m=-l}^{l}|f_{lm}|^2$. The spherical harmonics Y_l^m are continuous functions, but for computational applications, f is only sampled at N_Ω discrete angles. To create a shape signature for a 3D object, the shape is sampled at N_Ω angles and N_r radii, SH is calculated at each radius up to $l = L_{max}$, and the result is represented as a 2D grid of size $L_{max} \times N_r$. This SPHARM application described by Kazhdan et al. (2003) was more general shape classification using “clean” data (e.g. a set of 1890 “household” objects), but in noisy MRI data the SPHARM deals with noise automatically, since the noise does not appear in the lower frequencies that dominate shape descriptions. Many internal structures remain visible in data reconstructed from the signatures, while the signatures themselves require significantly less storage space than the original data. This general method was improved further by appropriate filtering (i.e. using exponentially weighted Fourier or spherical harmonics series, Chung et al. 2008a, 2007, 2008b). The weighting reduces a substantial amount of the so called ringing (or Gibbs) phenomenon and aliasing (or Moiré) patterns (Gelb, 1997)), both appearing because of relatively slow convergence of Fourier series when used for representing discontinuous or rapidly changing measurements.

Overall these modifications of the SPHARM method with filtering or exponential weighting (Chung et al., 2008a, 2007, 2008b) allowed successful parameterization of the cortical surface including characterization of the local difference in gray matter concentration. Nevertheless, techniques based on the SPHARM morphometry method – tensor-based

morphometry – uses the cortical surface already segmented out of noisy MRI data and quantifies the amount of gray matter only in a narrow layer along this surface via the concept of a local area element. Hence, the analysis can not be directly used for volumetric MRI data.

An extension of spherical harmonics decomposition that naturally allows incorporating of complete 3D volume data has been known in various areas of physics for quite a long time, i.e. in quantum physics for description of waveform solutions of the Shrödinger equation (Gersten, 1971), in atomic and nuclear physics for approximation of Coulomb scattering function (Barnett, 1996, 1981)), and in astrophysics for analyses of anisotropies of microwave background, as well as for quantum gravity (Abbott and Schaefer, 1986; Binney and Quinn, 1991; Leistedt et al., 2012).

In this paper we present the spherical wave decomposition (SWD) method, that combines angular-only basis functions of the SPHARM with spherical Bessel functions as the radial basis functions, forming the complete 3D basis. This basis is appropriate for expanding any function $f(r, \theta, \varphi)$ defined inside a sphere of radius a. The expansion coefficients have the advantage of allowing characterization of the internal structure simultaneously with the overall shape. Because they are not surface-based, there is no need to fix topological discrepancies or to provide surface based segmentation first. Thus this approach offers a more complete description of noisy volumetric data and is also more efficient to compute. We present timings for our implementation of the SWD method that confirm computational efficiency of the approach. We also describe further extension of the SWD approach to address the need of automated 3D volume segmentation.

3. Spherical Wave Decomposition Method

The basis functions for the spherical wave decomposition are composed of radial and angular parts. They can be obtained as eigensolutions of Laplace equation (or particular solution of Helmholtz's equation) $\nabla^2 f + k^2 f = 0$ (Lebedev, 1972), where the Laplacian ∇^2 is expressed in spherical coordinates as

$$\begin{aligned} \nabla^2 &= \nabla_r^2 + \tfrac{1}{r^2}\nabla_\Omega^2 \\ &= \tfrac{1}{r^2}\tfrac{\partial}{\partial r}\left(r^2\tfrac{\partial}{\partial r}\right) + \tfrac{1}{r^2\,sin\,\theta}\tfrac{\partial}{\partial\theta}\left(sin\,\theta\tfrac{\partial}{\partial\theta}\right) + \tfrac{1}{r^2\,sin^2\,\theta}\tfrac{\partial^2}{\partial\phi^2}. \end{aligned} \quad (2)$$

For a function $f(r, \theta, \varphi)$ defined inside a solid sphere of radius $r \le a$ the following expansion, obtained by separation of variables, is valid

$$f(r,\theta,\phi) = \sum_{n=1}^{\infty}\sum_{l=0}^{\infty}\sum_{m=-l}^{l} f_{lmn}\, R_{ln}(r)\, Y_l^m(\theta,\phi). \quad (3)$$

where the angular dependency is contained in the spherical harmonics $Y_l^m(\theta,\phi)$ – the eigensolution of the angular part of the Laplacian with the eigenvalues $\lambda_l = -l(l+1)$:

$$\nabla_\Omega^2 Y_l^m = \lambda_l Y_l^m. \quad (4)$$

The spherical harmonic Y_l^m of degree l and order m allows separation of the θ and φ variables when expressed using associated Legendre polynomials P_l^m of order m as

$$Y_l^m(\theta,\phi)=c_{l,m}\,P_l^m(\cos\theta)\,e^{-im\phi}, \quad (5)$$

where $c_{l,m}$ is the normalization constant

$$c_{l,m}=\sqrt{\frac{2l-1}{4\pi}\frac{(l-m)!}{(l+m)!}},$$

chosen to guarantee the orthonormality condition

$$\int_0^\pi\int_0^{2\pi} Y_l^m\,Y_{l'}^{m'\star}\sin\theta\,d\theta\,d\phi=\delta_{ll'}\,\delta_{mm'}.$$

The radial component $R_{ln}(r)$ of Eqn 3 is obtained as the eigenfunction of the radial Laplacian

$$\nabla_r^2 R_{ln}=-\left(k^2+\frac{\lambda_l}{r^2}\right)R_{ln}, \quad (6)$$

and can be expressed through the spherical Bessel function as

$$R_{ln}(r)=\frac{1}{\sqrt{N_{ln}}}j_l(k_{ln}r), \quad (7)$$

The normalization constants N_{ln} as well as the discrete spectrum wave numbers k_{ln} are determined by the choice of boundary conditions. For Dirichlet boundary condition, i.e. $f(r, \theta, \varphi) \equiv 0$ for $r \geq a$, they can be expressed as

$$N_{ln}=\frac{a^3}{3}j_{l+1}^2(x_{ln}), \quad k_{ln}=\frac{x_{ln}}{a}, \quad (8)$$

where $\{x_{ln}\}$ are ordered for $n \geq 1$ zeros of spherical Bessel function $j_l(x)$. With this choice of the discrete spectral numbers k_{ln} and the normalization constants N_{ln} the orthonormality conditions for $R_{ln}(r)$ reads

$$\int_0^a R_{ln}\,R_{ln'}\,r^2\,dr=\delta_{nn'}.$$

Using these basis function $R_{nl}(r)Y_l^m(\theta,\phi)$ the spherical Fourier coefficients f_{lmn} can be obtained as

$$f_{lmn}=\int_0^a\int_0^\pi\int_0^{2\pi} f(r,\theta,\phi)\;R_{nl}(r)\,Y_l^{m\star}(\theta,\phi)\,r^2\,dr\sin\theta\,d\theta\,d\phi. \quad (9)$$

As in SPHARM, a rotationally-invariant signature can be calculated directly from the coefficients f_{lmn} by taking the L_2-norm of all the f_{lmn} at each l and n:

$$S_{ln} = \sum_{m=-l}^{l} |f_{lmn}|^2. \quad (10)$$

The resulting signature, represented again as a 2D grid, now of size $L_{max} \times N_{max}$, where N_{max} is the number of spherical Bessel functions used in radial expansion, is purely in frequency space.

Straightforward calculations of the multiple radial shell SPHARM decomposition requires $O(N_r N_\Omega L_{max}^2)$ operations. For calculation of volumetric SWD spectra a separation of variables between the angular and the radial parts can be used. Still the brute force calculation of integrals in (9) results in even higher computational toll for the SWD than in the SPHARM – $O(N_r N_\Omega L_{max}^2 N_{max})$.

Fortunately, when taken independently both the angular and the radial parts allow use of fast $O(N \log N)$ transforms. The angular spherical harmonics decomposition was implemented using a divide and conquer approach and a fast Legendre transform (Driscoll and Healy, 1994; Healy et al., 1996, 2004; Mohlenkamp, 1999; Rokhlin and Tygert, 2006). For the radial spherical Bessel transform evaluation several different fast implementations are also available (Bisseling and Kosloff, 1985; Koval and Talman, 2010; Pettitt et al., 1993; Sharafeddin et al., 1992; Talman, 1978, 2009; Toyoda and Ozaki, 2010). In our implementation we followed Toyoda and Ozaki (2010) but replaced their recurrence formula with asymptotic expansion of the integral (see Appendix).

Volumetric MRI data are usually obtained on a Cartesian 3D grid. At the same time in order to be able to use the fast transforms both angular and radial parts should be defined on spherical grids with special grid placements. Therefore, the first step of a forward transform (i.e. transform to the frequency domain) and the last step of a backward transform (from the frequency domain) should provide a way of resampling the input and output 3D volume data from or to Cartesian grid, that is the following convolutions should be computed

$$f(\mathbf{r}) = \int\int\int F_x(\mathbf{x} - \mathbf{x}') f(\mathbf{x}') d^3 x',$$
$$f(\mathbf{x}) = \int\int\int F_r(\mathbf{r} - \mathbf{r}') f(\mathbf{r}') dV',$$

where $\mathbf{x} = (x, y, z)$ and $\mathbf{r} = (r, \theta, \varphi)$ are related through usual change of variables from Cartesian to spherical system of coordinates,

$$x = r \sin\theta \cos\phi, \quad y = r \sin\theta \sin\phi, \quad z = \cos\theta,$$

with the volume element $dV = r^2 dr \sin\theta d\theta d\varphi$. Different choice of resampling filters F_x and F_r (from simple nearest neighbor to complex multipoint interpolation) allows for balance between speed and quality.

4. Accuracy and Bandwidth

Our method was tested on high resolution MRI anatomical data of a normal human brain collected an a GE 3T MR750 Clinical Scanner using an inversion recovery *T*1-weighted 3D fast spoiled gradient recalled echo pulse sequence with parameters: flip angle $\alpha = 12°$, echo time *TE* = 3 *ms*, repetition time *TR* = 8 *ms*, matrix size = (*RL, AP, IS*) = (172×256×256), field of view *FOV* = (170 × 240 × 240) *mm* for a resolution of (1 × .938 × .938)*mm*. Characterization of this data as a function of SWD degrees L_{max} and N_{max} is shown in Figure 1 for progressively lower degrees of SWD transform. The largest degree (shown in Figure 1b) to exceed the physical dimensions of the original brain in order to confirm that a high degree SWD is capable of reconstructing all the details of the original dataset and produce visually indistinguishable result, and to show that our implementation is able to handle a large volume of frequency domain data ($> 300^3$ modes). Significant reduction in the degrees to $L_{max} = N_{max} = 100$, also produces a virtually indistinguishable brain. Even a relatively low resolution $L_{max} = N_{max} = 50$ with roughly a hundred times less information content than in the original volume is able to reproduce external as well as internal structure of the original brain.

Finally, the last two low resolution reconstructions (with degrees equal to 25 and 10) show the expected significant smoothing of both external and internal details. But even the lowest degree result, which uses less than $1/10^4$ of the original data, is able to capture and reproduce some important low resolution features of the original brain.

To illustrate the computational effectiveness of our SWD implementation we included timing of various stages of our implementation of SWD method for different degrees ($L_{max} = N_{max}$) of transform (Table 1). These timings were obtained for the same brain dataset using single thread Intel® Core™ i7-2760QM CPU 2.40GHz.

Simple nearest neighbor interpolation has been used for interpolation to Cartesian domain for all results reported in Table 1 (last column $F_r : \mathbf{r} \Rightarrow \mathbf{x}$) as well as for all transform degrees reported in Figure 1. For interpolation to spherical domain ($F_x : \mathbf{x} \Rightarrow \mathbf{r}$) we used an averaging over all the neighbors in the box obtained by mapping local spherical unit volume to Cartesian coordinates.

It is important to note that rows in Table 1 do not necessarily correspond to the work-flow of the SWD method. For example, it is possible to produce spherical interpolation using one resolution, then generate frequencies using a different degree, transform them back with yet another degree of transform, and finally arrive at Cartesian volumetric data with a different resolution. Hence, Table 1 is provided to illustrate scaling of various parts of the SWD computation with a change of the degree of transform. The most computationally demanding part of the method is the interpolation to spherical coordinates ($F_x : \mathbf{x} \Rightarrow \mathbf{r}$) that uses box averaging of neighbors. It took roughly 5.5 minutes to produce the largest 400^3 resolution in spherical domain. However, we emphasize that we are using double the reported resolution for all internal calculations, i.e. in this case the actual resolution was 800^3, that is 8 times larger. But a change of the execution time with a change of the degree L_{max} follows $O(L_{max}^3)$ pattern, i.e. it scales linearly with the total number of grid points processed.

Overall, the performance of the SWD method looks very competitive in comparison with the SPHARM, taking only on the order of seconds for $L_{max} = N_{max} \sim 100$, that is for calculation of all $L_{max}^2 \times N_{max}/2$ spectral coefficients. In contrast, single surface calculations of all the coefficients of SPHARM up to degree L_{max} =78 – that is $L_{max}^2/2$ total coefficients – takes more than few hours for direct numerical evaluation of integrals, and more than 5 minutes for the iterative residual fitting (IRF) algorithm of Chung et al. (2008a, 2007, 2008b).

We emphasize that the reported performance boost of the SWD approach relative to the fastest SPHARM implementation was not obtained at the expense of accuracy. On the contrary, analysis of root-mean-square (RMS) errors presented in the next section clearly shows that the SWD consistently produces several times lower RMS errors then the SPHARM in the same range of parameters. This means that the volume decomposition using complimentary radial and angular basis is clearly superior in term of accuracy to the angular only SPHARM decomposition.

To include smoothing effects (in addition to smoothing that can be provided by appropriate choice of resampling filters F_x and F_r) we also added the weighted Fourier series (WFS) representation in our spherical wave decomposition (Chung et al., 2007) by the inclusion of exponential weighting factors exp ($\lambda_l t$) in the original series (3):

$$f(\mathbf{r}_i) = \sum_{n=1}^{\infty} \sum_{l=0}^{\infty} \sum_{m=-l}^{l} e^{\lambda_l t} f_{lmn} R_{ln}(r_i) Y_l^m(\theta_i, \phi_i), \quad (11)$$

where $\lambda_l = -l(l+1)$ and t is a parameter which may be used to control the bandwidth. The results of the SWD with WFS are shown in Figure 2 for t=0.0001, 0.0005, 0.001, 0.005, 0.01 as well as for no smoothing with $t = 0$. By comparing all of them with Figure 1, the WFS smoothing with $0.01 \geq t \geq 0.001$ from the visual standpoint resembles limiting the degree of SWD transform somewhere below $L_{max} = 50$ level, whereas values of $0.001 > t \geq 0.0001$ correspond to L_{max} values between 50 and 100.

To illustrate that the inclusion of WFS reduces the substantial amount of the Gibbs phenomenon – ringing artifacts associated with the slow convergence of a Fourier series (Gelb, 1997) – we applied the SWD both with and without the WFS to a slowly converging SWD representation of a 3-D step-like function (Figure 3). For comparison with Chung et al. (2008a) we used the same set of parameters for the degree ($L_{max} = N_{max}$=78) and the bandwidth ($t = 0.0001$) of the SWD transform. The weighted SWD shown in Figure 3b clearly has less ringing artifacts than the original SWD (Figure 3a), although the reduction is not as profound as in the weighted SPHARM of the same degree and bandwidth, probably due to higher overall accuracy of the SWD approach and additional smoothing provided by the resampling filters F_x and F_r.

Analysis of quantitative procedure of finding optimal degree of SWD transform that is characteristics of some particular level of smoothing is provided in the next section.

5. Choice of Optimal Order of SWD Transform

To estimate how well the SWD with some preselected degrees L_{max} and N_{max} will represent any particular dataset the root mean square deviation can be used. Because increasing the angular L_{max} and the radial N_{max} degrees of SWD increases not only the goodness-of-fit, but also the number of coefficients to be estimated, finding the optimal degree where this increase in the number of parameters is warranted by the goodness-of-fit is very important. This is even more important for the SWD than in the single surface SPHARM approach (Chung et al., 2008a, 2007, 2008b), as the growth of coefficients now happens cubically, not quadratically.

Although in the SWD the angular and the radial degrees can be changed independently, the number of zeros of the spherical Bessel function that fall inside the sphere of radius a corresponds to the number of zeros in latitudinal or longitudinal directions when $L_{max} \sim N_{max}$. Hence, for a purpose of finding the optimal degree order we will assume that $N_{max} = L_{max}$.

Following Chung et al. (2007) we will assume that distribution of the Fourier coefficients f_{lmn} can be approximated to follow normal distribution $N(\mu_{lmn}, \sigma_l^2)$ with equal variance σ_l within the same degree. This corresponds to the following $k-1$ degree model

$$f_{k-1}(\mathbf{r}_i) = \sum_{n=1}^{k-1} \sum_{l=0}^{k-1} \sum_{m=-l}^{l} e^{-l(l+1)t} \mu_{lmn} R_{ln}(r_i) Y_l^m(\theta_i, \phi_i) + \varepsilon(\mathbf{r}_i) \quad (12)$$

where $\boldsymbol{\varepsilon}$ is a zero mean isotropic Gaussian random field. Then we can test if increasing the degree of the model above $k-1$ is statistically significant by testing the null hypothesis

$$H_0: \mu_{lmn} = 0 \quad for \quad l = k, n = k, |m| \leq k. \quad (13)$$

For the construction of test statistic we use the residual sum of squares (RSS) for the $(k-1)$ degree model f_{k-1}, that is

$$RSS_{k-1} = RSS_{(f_{k-1})} = \sum_{i=1}^{N} (f(\mathbf{r}_i) - f_{k-1}(\mathbf{r}_i))^2. \quad (14)$$

In Figure 4 is plotted the root-mean-square-deviation ($RMSD_k = \sqrt{RSS_k/N}$) as a function of k (that is the SWD degree $L_{max} = N_{max}$) for the brain reconstructions shown in Figure 2 obtained for different values of exponential smoothing parameter t. The overall behavior seems consistent with the SPHARM, showing that initial fast decrease of the root mean square deviation gradually slows down and flattens out. The value of error in the flat region as well as the degree where the transition to the flat region occurs depends on the smoothing parameter t, also consistent with the SPHARM. The important difference of the SWD is that it consistently shows several times lower RMS errors then the SPHARM in the same range of L_{max} and t parameters. It means that volume decomposition using complimentary radial

and angular basis is clearly superior in term of accuracy to the single surface only (or even the shell of surfaces) angular SPHARM decomposition.

We modified the test statistic used in SPHARM to account for different number of ”groups” and ”observations” used in each of the methods:

$$F=\frac{(RSS_{k-1}-RSS_k)/(3k^2+k)}{RSS_{k-1}/(N-(k+1)^2k)}\sim F_{3k^2+k,N-(k+1)^2k}, \quad (15)$$

The resulting distribution is again the *F*-distribution, with different values of the degrees-of-freedom $(3k + 1)k$ and $N - k(k + 1)^2$. The optimal SWDdegree can be obtained by computing the *F* statistic for each degree *k* up to the point when the corresponding P-value becomes bigger than the prespecified significance α. Our results for $\alpha = 0.01$ seem to be pretty close to the SPHARM values, i.e. for the bandwidth $t = 0.0001$ the optimal SWD degree has been determined to be $k = 80$ vs $k = 78$ for the SPHARM.

6. Using SWD for Volume Segmentation

One important difference between the SWD and the SPHARM methods lies in the possibility of a relatively simple and straightforward modification of the SWD to naturally and effectively handle the very complex task of volume segmentation. Segmentation is not tractable by the SPHARM method itself because it requires processing of the whole volumetric data but SPHARM is based on a partial decomposition valid only on the unit sphere. Thus segmentation must be performed (either by hand or by using additional specialized semi-automated segmentation tools) *before* the SPHARM method can even be applied to new volumetric data.

On the other hand the SWD method is based on an expansion of the whole volume in a series of orthogonal basis functions, therefore it can be reformulated to reconstruct not just the internal volume of the input 3D data, but to produce and emphasize all the interfaces or transitions that exist inside the volume. Mathematically this procedure can be described by taking the square of the gradient of the expansion $|\nabla f(r, \theta, \varphi)|^2$, similar to the approach taken by various edge detection techniques used in 2D image processing. This edge detection is essentially the first and the most important step of almost any segmentation technique used in 2D, and the quality of edge detection is crucial for overall success of segmentation process. Using Fourier expansion of 2D images this gradient calculations can be improved significantly (Gelb and Cates, 2009) both in accuracy and in computational efficiency.

The SWD method is essentially a three-dimensional variant of a Fourier decomposition and most of the results of conventional Fourier series analysis can be transferred (with appropriate modifications) to the spherical wave series. Therefore, the SWD coefficients can be used for interface detection in 3D by efficient and accurate computation of the gradient square. In spherical coordinates the gradient has the following components

$$\nabla_r = \frac{\partial}{\partial r}, \quad \nabla_\theta = \frac{1}{r}\frac{\partial}{\partial \theta}, \quad \nabla_\phi = \frac{1}{r\ sin\,\theta}\frac{\partial}{\partial \phi}, \quad (16)$$

and in order to efficiently compute $|\nabla f(r, \theta, \varphi)|^2$ instead of the original volume function $f(r, \theta, \varphi)$ we have to apply each of these components to the expansion (3).

Using recurrence relations for derivatives of the associated Legendre polynomials $P_l^m(x)$

$$\frac{d}{dx}P_l^m(x) = \frac{1}{1-x^2}\left[-lx\,P_l^m(x) + (l+m)\,P_{l-1}^m(x)\right], \quad (17)$$

and for derivatives of the spherical Bessel function $j_l(x)$

$$\frac{d}{dx}j_l(x) = j_{l-1}(x) - \frac{l+1}{x}j_l(x), \quad (18)$$

we can update the expansion coefficients and obtain expressions for the gradient components as a new SWD series along each of the orthogonal coordinates:

$$\nabla_\phi f(r,\theta,\phi) = \frac{1}{r\ sin\,\theta}\sum_{n=1}^{\infty}\sum_{l=0}^{\infty}\sum_{m=-l}^{l}(-im)\,f_{lmn}\,R_{ln}(r)\,Y_l^m(\theta,\phi) \quad (19)$$

$$\begin{aligned}\nabla_\theta f(r,\theta,\phi) &= \frac{cos\,\theta}{r\ sin\,\theta}\sum_{n=1}^{\infty}\sum_{l=0}^{\infty}\sum_{m=-l}^{l} l f_{lmn}\,R_{ln}(r)\,Y_l^m(\theta,\phi) \\ &- \frac{1}{r\ sin\,\theta}\sum_{n=1}^{\infty}\sum_{l=0}^{\infty}\sum_{m=-l}^{l}(l+m)\ f_{(l+1)mn}\,R_{ln}(r)\,Y_l^m(\theta,\phi)\end{aligned} \quad (20)$$

$$\begin{aligned}\nabla_r f(r,\theta,\phi) &= \sum_{n=1}^{\infty}\sum_{l=0}^{\infty}\sum_{m=-l}^{l} k_{ln}\,f_{lm(n+1)}\,R_{ln}(r)Y_l^m(\theta,\phi) \\ &- \frac{1}{r}\sum_{n=1}^{\infty}\sum_{l=0}^{\infty}\sum_{m=-l}^{l}(n+1)\ f_{lmn}\,R_{ln}(r)\,Y_l^m(\theta,\phi)\end{aligned} \quad (21)$$

The same SWD procedure described in the previous section can be used to transform these coefficients to spherical and then Cartesian domain. Hence five SWD transforms will be needed to compute the gradient square.

An example of the derivatives in human anatomical data is shown in Figure 5. The bottom (derivative) panel clearly shows detection of interfaces between various tissues present in the original anatomical volumetric data, including interfaces between gray and white matter.

This Fourier based approach for obtaining expressions for the gradient components has several advantages over direct numerical differentiation in the spatial domain. First of all, due to the multiscale nature of the SWD algorithm it easily allows controlling the scale of the gradients involved in the edge detection process. Moreover, numerical differentiation of noisy data in the spatial domain has inherently low accuracy, whereas the Fourier based algorithm can significantly improve the accuracy by appropriate choice of filtering.

In practice, fully automated segmentation requires a combination of methods that not only characterizes the shapes of the internal structures, but incorporates some prior information about their spectrum, spatial scales, and spatial distributions. This combination can include the interfaces from the volume gradient to find an initial estimate for intensity thresholds and number of intensity clusters. The low frequency interfaces (actually their positions) can then be included in some sort of topological analysis. And finally the high frequency interface data can be used to facilitate topological closure of found low frequency clusters that is to update and generate detailed structures.

Such an analysis is beyond the scope of the current paper and so for the purpose of this paper we did not analyze a topological structure of the gradient generated interface surface yet. However, the potential our method holds for automatic segmentation can be demonstrated using the derivative map surface for the brain volumetric data that we used in the previous sections for analyses of the SWD accuracy and bandwidth (Figure 1a). We assumed a bimodal structure of the volumetric intensities, but in contrast to most classification techniques we did not make any assumptions about type of a distribution for each of the modes (i.e. we did not ask it to be Gaussian). We only assumed that the modes are well separated and applied the derivative map to estimate an intensity threshold I_t by calculating an average intensity inside all regions with large values of intensity gradient

$$I_t = \sum_{|\nabla f| > \nabla_f} f(x,y,z) \Big/ \sum_{|\nabla f| > \nabla_f} 1, \quad (22)$$

where $\nabla_f = \overline{|\nabla f|}$. This simplified illustrative procedure still allowed us to obtain in a completely automatic manner accurate segmentation between gray and white matter, independently shown in Figure 6 (gray matter) and Figure 7 (white matter).

We would like to emphasize that all types of SWD based analyses described in the previous sections (including weighted Fourier smoothing, optimal SWD order and volume morphometry/complexity) are also applicable to these segmented out and independently represented brain structures. Thus, the average gray matter density, the cortical thickness, as well as various local abnormalities, can be accurately calculated directly from the volumetric data on different scales (i.e. using different degrees of smoothness). This is in contrast to the SPHARM, where both the gray matter density and the cortical thickness can only be approximated through a distance map between independently fitted inner and outer cortical surfaces (Chung et al., 2007), a process that is prone to various sources of errors (the most important are errors from surface registration, mesh construction and discrete thickness computation), and is very sensitive to presence of noise.

To test the efficacy of our approach in real life applications as well as to compare with the current state-of-the-art methods we conducted a complete analysis work-flow of brain segmentation/characterization task using our original 3D brain dataset (Figure 1a) as an input to FreeSurfer/SPHARM combination. As the SPHARM on its own is unable to analyze volumetric data, the typical analysis work-flow requires as a first step preprocessing of the volumetric data with FreeSurfer (Dale et al., 1999). At this stage we extracted white matter surface using all the required steps of the standard FreeSurfer processing, i.e

segmentation, inflation, registration, fitting to sphere, etc. The total FreeSurfer processing took more than 12 hours to obtain a single hemisphere white matter surface.

The resulting white matter surface of the left hemisphere has been used afterwards as an input to several different stages of the SPHARM analysis using codes from http://www.stat.wisc.edu/~mchung/softwares/weighted-SPHARM/weighted-SPHARM.html. The first SPHARM step is to construct the spherical harmonics representation and save it into a hard drive (~ 2.86 GB). This step took around 7 minutes for generating all the harmonics up to L_{max}=85. (L_{max}=85 has been chosen due to the inability of the SPHARM to produce higher degree expansion giving us "matrix is singular to working precision" error for any degree above 85). The WFS smoothing step (SPHARMsmooth2) of the SPHARM took about half an hour using the same degree L_{max}=85. And finally generation of the smoothed white matter surface from a set of Fourier coefficients (SPHARMrepresent2) took around 20 minutes. The overall processing of the left hemisphere white matter surface took close to 14 hours (the processing times are summarized in Table 2). The total FreeSurfer processing of both hemispheres as well as the gray matter surfaces took almost a day ($\gtrsim$ 23 hours).

Figure 8 shows the 3D views of both the SPHARM and the SWD white matter extraction results. The details as well as the quality of the segmentation seems to be comparable for the SPHARM (a) and for the SWD (b), but topological defects produced by a single sphere inflation procedure of FreeSurfer followed by smoothing of the SPHARM are clearly visible in the SPHARM surface (Figure 8c) and absent in the SWD (Figure 8d).

The reason for these topological defects can become more obvious by looking at several slices of the volumetric data with the SPHARM/FreeSurfer white matter surface overlaid. Figures 9a and b show original FreeSurfer segmentation results (blue), and Figures 9c and d show the final surface obtained with SPHARM smoothing (red). The yellow accented area shows the same defect that was marked by yellow in the previous Figure 8a. Another defect area, marked green, is located deep inside the volume. The bridging of both of these areas results in topologically incorrect surface closure and produces convex region that actually encompass hollow area inside this topologically closed white matter region. This erroneous bridging is absent on slides of volumetric SWD white matter (Figures 9e and f).

To quantitatively characterize an amount of topological defects that are present in the SPHARM/FreeSurfer white matter surface (Figure 8a) and in the isosurface of the volumetric SWD white matter (Figure 8b) we estimated the Euler characteristic (sometimes also called the Euler-Poincaré characteristic) for the trianlulated meshes obtained in both analyses.

The Euler characteristic χ was classically defined for the surfaces of polyhedra, according to the formula (Spanier, 1994)

$$\chi = V - E + F \quad (23)$$

where V, E, and F are respectively the numbers of vertices (corners), edges and faces in the given polyhedron. Any convex polyhedron's surface has Euler characteristic $\chi = 2$.

The SPHARM/FreeSurfer white matter mesh shown in Figure 8a has 161532 vertices, 323060 (triangular) faces and 420506 edges, thus giving the Euler characteristic $\chi_{FreeSurfer}$ equals to 64086. The SWD mesh shown in Figure 8b has 166314 vertices, 332680 faces (triangular as well) and 488207 edges. The Euler characteristic χ_{SWD} is then equal to 10787.

An ideal regular white matter genus zero surface (that it is homologous to a sphere) should have χ=2, therefore, the SWD provides significant (almost 6-fold) decrease in overall number of topological artifacts.

7. SWD Application to Clinical Brain Morphometry

To further validate our method as well as to show its competitiveness not only in research but also in clinical settings, we used the work-flow entirely based on our SWD approach to replicate the results of a recent analysis of differential effects of binge drinking on the brain morphometry of adolescent males and females (Lisdahl et al., 2013; Squeglia et al., 2012). These results establish links between cortical thickness in several areas of the brain to repeated binge drinking, hence confirming the potentially deleterious effects of binge drinking on adolescent brain development, as it is known that early adolescent cortical thinning is related to better neuropsychological performance (Squeglia et al., 2013).

We used the same set of high-resolution anatomical images (Squeglia et al., 2012) collected at the UCSD Keck fMRI Center from a 3-Tesla CXK4 short bore Excite-2 MR system (General Electric, Milwaukee, WI) with an eight-channel phase-array head coil. Scan sessions involved a 10-s scout scan with slice selection covering the whole brain, followed by a sagittally acquired high-resolution 3D T1-weighted anatomical MRI that lasted 7 min and 26 s (FOV 24 cm, 256 × 256 × 192 matrix, 0.94 × 0.94 × 1 mm voxels, 176 slices, TR=20 ms, TE=4.8 ms; flip angle 12°). Two representative scans both from the study group (14 female and 15 make binge drinkers) and from the healthy control group (15 females and 15 males) are shown in Figures 10a and b.

The complete processing of high-resolution anatomical volumetric datasets was done by our SWD framework and no other preprocessing steps were necessary. The spherical wave gradient approach described above was used for the automated skull stripping as well as for the white/gray matter segmentation (Figures 10c,d,e and f). No time consuming surface fitting/ topology correction steps were required for the cortical thickness calculations. The average cortical thickness for the left frontal poles (Figures 10e and f) have been derived from the volumetric gray matter data as a ratio of a number of all gray matter voxels (G) to a number of boundary voxels in gray/white matter boundary (∂G),

$$H_{cortical} = \sum_{f(x,y,z)\in G} 1 \Big/ \sum_{f(x,y,z)\in \partial G} 1, \quad (24)$$

where the gray/white matter boundary ∂G is defined by all voxels in G that has at least one neighbor from the white matter region. The angular extent of left frontal pole has been specified by a common for all datasets range of spherical coordinates ($\theta_1 < \theta < \theta_2$ and $\varphi_1 < \varphi < \varphi_2$).

The cortical thickness obtained from our analysis seems to correlate well with the results of the original study but our approach produces slightly better mean separation between study and control groups (~ 0.1*mm*). For example, the two left frontal pole samples shown in Figures 10e and f, were found to have the cortical thickness of 2.80mm and 3.52mm (vs 2.96mm and 3.51mm) and were correctly placed in normal and abnormal female groups (with the mean cortical thickness and the standard deviation of 3.24±0.19mm and 3.00±0.23 respectively). Analysis of each sample using the SWD framework takes on the order of minutes, rather than the tens of hours required for the original approach.

We would like to emphasize that the original analysis, presented in Squeglia et al. (2012), using FreeSurfer for independent left and right hemispheres white matter segmentation, required a significant amount of both computer and human inspection time spent fixing the topology of the segmentation, in order for it to be homologous to a sphere. The volumetric based filtering provided by the SWD using interrelated scales in both radial (spherical Bessels) and tangential (spherical harmonics) parts is able to reduce a number of simple geometrical artifacts (e.g. needles), that can be further minimized by filtering out the high-frequency terms with, for example, a simple Fourier transformation low-pass filter (of course, at the expense of creating a convolved image, where edges are also blurred).

More importantly, the volumetric SWD based analysis is able to reduce the true topological defects, i.e. those defects that prevent the surface that has genus zero to be inflated to a sphere due to spurious handles and holes, resulting is relatively regular surface borders of both white and gray matter volumes (as can be seen from Figures 10c,d,e and f). Thus, in contrast to a simple Fourier transformation, the volumetric SWD transform method favors the spherical nature of the cortical band. As a result there was no need for the topology fixing step anywhere in our analysis, as our expression for the cortical thickness directly involves volumetric data that are “regularized” in some sense by the volumetric SWD reconstruction and does not require the expensive surface fitting/inflation step.

8. Conclusion

We have presented a novel spherical wave decomposition (SWD) method that allows compact representation, characterization, automatic segmentation and morphometry analysis of complex shapes embedded within volumetric data. The method is very general and thus applicable to a wide range of applications. In particular, the method is appropriate for efficient quantitative analysis of volumetric magnetic resonance imaging data.

The SWD representation uses a direct expansion of volumetric data in a linear combination of basis functions that include both angular (spherical harmonics) and radial (spherical Bessel functions) parts. The 3D descriptors are easily archived and facilitate statistical comparison at multiple spatial scales: low frequency information describes gross shape, while high frequency information captures more detail as well as internal structures.

In contrast to surface based methods, the SWD approach does not require an initial segmentation of a surface and a subsequent inflation of this surface to satisfy the uniqueness or stability of subsequent surface fitting algorithms. The surface methods are inefficient and time consuming because of the need for segmentation prior to fitting and the

computationally intensive inflation process, the latter of which being also a significant source of errors due to creation of topological defects.

Our implementation of the SWD method is based on several fast transforms for spherical harmonics and spherical Bessel functions and, therefore, is significantly faster than the surface based methods, but at the same time provides significantly higher accuracy. The fast transforms for spherical Bessel functions are based on our novel expression for asymptotic expansion as $1/k^n$ series of the standard sine and cosine Fourier transforms and rearrangement of coefficients obtained by the standard FFTs afterwards.

Overall, the SWD method seems to be uniquely positioned to provide an effective, accurate and robust approach for morphology characterization, segmentation, and comparative morphometry for both basic neuroscience studies on comparative brain anatomy and clinical studies of disease characterization and progression in humans, and for a broad range of studies in comparative biology.

Acknowledgments

We thank S. Tapert and L. Squeglia for generously providing access to binge drinking brain morphometry study MRI data. We are also indebted to two anonymous reviewers for a number of thoughtful comments and suggestions. LRF and VLG were supported by NSF grants DBI-1143389, DBI- 1147260, EF-0850369, PHY-1201238 and NIH grant R01 MH096100. All MRI scans used in Section 7 were supported by NIH grant R01 AA13419, PI: Tapert.

Appendix A. Fast spherical Bessel transform

The integral representation of the spherical Bessel function is given by

$$j_l\left(z\right)=\frac{1}{2i^l}\int_{-1}^{1}e^{izt}\,P_l\left(t\right)dt, \quad \text{(A.1)}$$

where $P_l(t)$ is the Legendre polynomials. By substituting Eqn A.1 into radial part of the SWD transform

$$f\left(k,\theta,\phi\right)=\int_0^\infty j_l\left(kr\right)\,f\left(r,\theta,\phi\right)r^2dr, \quad \text{(A.2)}$$

and integrating by parts, the transform can be rewritten as follows:

$$\begin{aligned} f\left(k,\theta,\phi\right) &= \frac{1}{2i^l} && \int_{-1}^{1}dt\,P_l\left(t\right)\int_0^\infty r^2\,dre^{ikrt}f\left(r,\theta,\phi\right) \\ &= \frac{1}{2i^l} && \int_{-1}^{1}dt\,P_l\left(t\right)\frac{1}{ik}\frac{d}{dt}\int_0^\infty rdre^{ikrt}\,f\left(r,\theta,\phi\right) \\ &= \frac{1}{2i^l} && \left[\frac{1}{ik}P_l\left(t\right)\int_0^\infty rdre^{ikrt}f\left(r,\theta,\phi\right)\Big|_{-1}^{1}-\right. \\ & && \left.\frac{1}{ik}\int_{-1}^{1}dt\,P_l'\left(t\right)\int_0^\infty rdre^{ikrt}f\left(r,\theta,\phi\right)\right] \\ &= \frac{1}{2i^l} && \left[\sum_{n=0}^{N}\frac{(-1)^n}{(ik)^{n+1}}P_l^{(n)}\left(t\right)\int_0^\infty r^{1-n}dre^{ikrt}f\left(r,\theta,\phi\right)\Big|_{-1}^{1}-\right. \\ & && \left.\frac{(-1)^N}{(ik)^{N+1}}\int_{-1}^{1}dt\,P_l^{(N+1)}\left(t\right)\int_0^\infty r^{1-N}dre^{ikrt}f\left(r,\theta,\phi\right)\right]. \end{aligned} \quad \text{(A.3)}$$

As derivative $P_l^{(N)}(t)$ vanishes for $N > l$, the summation in Eqn A.3 only goes to $N = l$, that is

$$f(k,\theta,\phi) = \frac{1}{2i^l}\sum_{n=0}^{l}\frac{(-1)^n}{(ik)^{n+1}}P_l^{(n)}(t)\int_0^\infty r^{1-n}dre^{ikrt}f(r,\theta,\phi)\Big|_{-1}^{1}. \quad \text{(A.4)}$$

The integrals in Eqn A.4 evaluated at $t = \pm 1$ represent the one dimensional half plane Fourier transforms of $f(r, \theta, \varphi)$ multiplied by various powers of r. Using the parity property of the Legendre polynomials $P_l^{(n)}(-t) = (-1)^{l+n}P_l^{(n)}(t)$ the Fourier integrals in Eqn A.4 can be rewritten through the standard sine and cosine Fourier series instead:

$$f(k,\theta,\phi) = \sum_{n=0}^{l}\frac{P_l^{(n)}(1)}{k^{n+1}} \times \begin{cases} (-1)^{\left\lfloor\frac{l-n}{2}\right\rfloor}\int_0^\infty r^{1-n}\,dr\,sin\,(kr)\,f(r,\theta,\phi), & l+n\ is\ even \\ (-1)^{\left\lfloor\frac{l-n+1}{2}\right\rfloor}\int_0^\infty r^{1-n}\,dr\,cos\,(kr)\,f(r,\theta,\phi), & l+n\ is\ odd \end{cases} \quad \text{(A.5)}$$

where $\lfloor x \rfloor$ denotes *floor* (x), i.e. the largest integer that does not exceed x.

It is clear from Eqn A.5 that all the coefficients of the spherical Bessel transform can be obtained by rearrangement of coefficients of sine and cosine Fourier transforms of $f(r, \theta, \varphi)$ multiplied by powers of radius r^{ε} with integer exponent ε decreasing from 1 to $1 - l$.

However, for the purpose of efficient numerical implementation we do not compute all the terms in summation of Eqn A.5. Instead, we choose rather low upper limit of summation ($N = 0$ or 1) and evaluate the residual (the last term in Eqn A.3) using numerical integration, progressively evaluating the terms until they are smaller than some prescribed threshold. Because the Fourier expansion decreases not slower than k_{-1} (even for discontinuous functions) and taking into account an additional multiplication by a factor $1/k^{N+1}$, this seems to be always possible even despite the presence of large derivative of the Legendre polynomials $P_l^{(N+1)}$, although the rigorous mathematical verification of this behavior lies beyond the scope of this paper.

References

Abbott LF, Schaefer RK. A general, gauge-invariant analysis of the cosmic microwave anisotropy. ApJ. 1986; 308:546–562.10.1086/164525

Atkins MS, Mackiewich BT. Fully automated hybrid segmentation of the brain. Handbook of Medical Imaging, Processing and Analysis. 2000:171–183.

Barnett A. The calculation of spherical Bessel functions and Coulomb functions. Computational Atomic Physics: Electron and Positron Collisions with Atoms and Ions. 1996:181–202.

Barnett AR. An algorithm for regular and irregular Coulomb and Bessel functions of real order to machine accuracy. Computer Physics Communications. 1981; 21:297–314.10.1016/0010-4655(81)90011-4

Barra V, Boire JY. Tissue segmentation on MR images of the brain by possibilistic clustering on a 3D wavelet representation. J Magn Reson Imaging. 2000; 11:267–278. [PubMed: 10739558]

Barra V, Boire JY. Automatic segmentation of subcortical brain structures in MR images using information fusion. IEEE Trans Med Imaging. 2001; 20:549–558. [PubMed: 11465462]

Barra V, Boire JY. Segmentation of fat and muscle from MR images of the thigh by a possibilistic clustering algorithm. Comput Methods Programs Biomed. 2002; 68:185–193. [PubMed: 12074845]

Binney J, Quinn T. Gaussian random fields in spherical coordinates. MNRAS. 1991; 249:678–683.

Bisseling R, Kosloff R. The fast Hankel transform as a tool in the solution of the time dependent Schrödinger equation. Journal of Computational Physics. 1985; 59:136–151.

Brechbühler C, Gerig G, Kübler O. Parametrization of Closed Surfaces for 3-D Shape Description. Computer Vision and Image Understanding. 1995; 61:154–170.

Chung MK, Dalton KM, Davidson RJ. Tensor-Based Cortical Surface Morphometry via Weighted Spherical Harmonic Representation. IEEE Trans Med Imaging. 2008a; 27:1143–1151. [PubMed: 18672431]

Chung MK, Dalton KM, Shen L, Evans AC, Davidson RJ. Weighted Fourier Series Representation and Its Application to Quantifying the Amount of Gray Matter. IEEE Trans Med Imaging. 2007; 26:566–581. [PubMed: 17427743]

Chung MK, Hartley R, Dalton K, Davidson RJ. Encoding cortical surface by spherical harmonics. Statistica Sinica. 2008b; 18:1269.

Cocuzzo D, Lin A, Ramadan S, Mountford C, Keshava N. Algorithms for characterizing brain metabolites in two-dimensional in vivo MR correlation spectroscopy. Conf Proc IEEE Eng Med Biol Soc. 2011; 2011:4929–4934. [PubMed: 22255444]

Dale AM, Fischl B, Sereno MI. Cortical surface-based analysis. I Segmentation and surface reconstruction. Neuroimage. 1999; 9:179–194. [PubMed: 9931268]

Driscoll JR, Healy DM. Computing Fourier transforms and convolutions on the 2-sphere. Advances in applied mathematics. 1994; 15:202–250.

Gelb A. The resolution of the Gibbs phenomenon for spherical harmonics. Mathematics of Computation. 1997; 66:699–717.

Gelb A, Cates D. Segmentation of images from fourier spectral data. Commun Comput Phys. 2009; 5:326–349.

Gersten A. Wavefunction Expansion in Terms of Spherical Bessel Functions. Journal of Mathematical Physics. 1971; 12:924–929.10.1063/1.1665682

He Q, Karsch K, Duan Y. Semi-automatic 3D segmentation of brain structures from MRI. Int J Data Min Bioinform. 2011; 5:158–173. [PubMed: 21544952]

Healy D Jr, Rockmore D, Kostelec PJ, Moore SSB. FFTs for the 2-Sphere - Improvements and Variations. The Journal of Fourier Analysis and Applications. 1996; 9:341–385.

Healy DM Jr, Kostelec PJ, Rockmore DN. Towards Safe and Effective High-Order Legendre Transforms with Applications to FFTs for the 2-sphere. Adv Comput Math. 2004; 21:59–105.

Kazhdan, MM.; Funkhouser, TA.; Rusinkiewicz, S. Rotation Invariant Spherical Harmonic Representation of 3D Shape Descriptors. In: Kobbelt, L.; Schröder, P.; Hoppe, H., editors. Symposium on Geometry Processing; Eurographics Association; 2003. p. 156-164.

Kiebel SJ, Goebel R, Friston KJ. Anatomically informed basis functions. Neuroimage. 2000; 11:656–667. [PubMed: 10860794]

Klauschen F, Goldman A, Barra V, Meyer-Lindenberg A, Lundervold A. Evaluation of automated brain MR image segmentation and volumetry methods. Hum Brain Mapp. 2009; 30:1310–1327. [PubMed: 18537111]

Klein A, Andersson J, Ardekani BA, Ashburner J, Avants B, Chiang MC, Christensen GE, Collins DL, Gee J, Hellier P, et al. Evaluation of 14 nonlinear deformation algorithms applied to human brain MRI registration. Neuroimage. 2009; 46:786. [PubMed: 19195496]

Koval P, Talman JD. Update of spherical Bessel transform: FFTW and OpenMP. Computer Physics Communications. 2010; 181:2212–2213.

Lebedev, N. Special functions and their applications. In: Silverman, Richard A., editor. Unabridged and corrected republication. Dover Publications, Inc.; New York: 1972. Revised edition, translated from the Russian

Leistedt B, Rassat A, Réfrégier A, Starck JL. 3DEX: a code for fast spherical Fourier-Bessel decomposition of 3D surveys. A&A. 2012; 540:A60. arXiv:1111.3591. 10.1051/0004-6361/201118463

Li, S. Eklundh, JO., editor. Markov random field models in computer vision; Computer Vision ECCV '94 Springer Berlin Heidelberg, of Lecture Notes in Computer Science. 1994. p. 361-370.URL: http://dx.doi.org/10.1007/BFb0028368

Liang Z, MacFall J, Harrington D. Parameter estimation and tissue segmentation from multispectral MR images. Medical Imaging, IEEE Transactions on. 1994; 13:441–449.10.1109/42.310875

Lin GC, Wang WJ, Kang CC, Wang CM. Multispectral MR images segmentation based on fuzzy knowledge and modified seeded region growing. Magn Reson Imaging. 2012; 30:230–246. [PubMed: 22133286]

Lisdahl KM, Thayer R, Squeglia LM, McQueeny TM, Tapert SF. Recent binge drinking predicts smaller cerebellar volumes in adolescents. Psychiatry Res. 2013; 211:17–23. [PubMed: 23154095]

Mangin JF, Frouin V, Bloch I, Régis J, López-Krahe J. From 3D magnetic resonance images to structural representations of the cortex topography using topology preserving deformations. Journal of Mathematical Imaging and Vision. 1995; 5:297–318.

Mohlenkamp MJ. A fast transform for spherical harmonics. Journal of Fourier analysis and applications. 1999; 5:159–184.

Pachai, C.; Zhu, YM.; Guttmann, CRG.; Kikinis, R.; Jolesz, FA.; Gimenez, G.; Froment, JC.; Confavreux, C.; Warfield, SK. Unsupervised and Adaptive Segmentation of Multispectral 3D Magnetic Resonance Images of Human Brain: A Generic Approach. Niessen, WJ.; Viergever, MA., editors. MICCAI, Springer; 2001. p. 1067-1074.

Pedoia, V.; Binaghi, E. Automatic MRI 2D brain segmentation using graph searching technique. International Journal for Numerical Methods in Biomedical Engineering. 2012. URL: http://dx.doi.org/10.1002/cnm.2498

Pettitt BA, Danchura W, Labun D. Spherical Bessel Transforms. Journal of Computational Physics. 1993; 105:178–181.10.1006/jcph.1993.1064

Pham DL, Prince JL. An adaptive fuzzy C-means algorithm for image segmentation in the presence of intensity inhomogeneities. Pattern Recognition Letters. 1999; 20:57–68.

Pham DL, Xu C, Prince JL. A Survey of Current Methods in Medical Image Segmentation, in: Annual Review of Biomedical Engineering. 2000; 2:315–338.

Popuri K, Cobzas D, Murtha A, Jagersand M. 3D variational brain tumor segmentation using Dirichlet priors on a clustered feature set. Int J Comput Assist Radiol Surg. 2012; 7:493–506. [PubMed: 21833491]

Razlighi QR, Orekhov A, Laine A, Stern Y. Causal Markov random field for brain MR image segmentation. Conf Proc IEEE Eng Med Biol Soc. 2012; 2012:3203–3206. [PubMed: 23366607]

Rokhlin V, Tygert M. Fast algorithms for spherical harmonic expansions. SIAM Journal on Scientific Computing. 2006; 27:1903–1928.

Sharafeddin OA, Ferrel Bowen H, Kouri DJ, Hoffman DK. Numerical Evaluation of Spherical Bessel Transforms via Fast Fourier Transforms. Journal of Computational Physics. 1992; 100:294.10.1016/0021-9991(92)90236-R

Spanier, E. Mathematics subject classifications. Springer; 1994. Algebraic Topology. URL: http://books.google.com/books?id=h-wc3TnZMCcC

Squeglia LM, Jacobus J, Sorg SF, Jernigan TL, Tapert SF. Early adolescent cortical thinning is related to better neuropsychological performance. J Int Neuropsychol Soc. 2013; 19:962–970. [PubMed: 23947395]

Squeglia LM, Sorg SF, Schweinsburg AD, Wetherill RR, Pulido C, Tapert SF. Binge drinking differentially affects adolescent male and female brain morphometry. Psychopharmacology (Berl). 2012; 220:529–539. [PubMed: 21952669]

Suri JS. Two-dimensional fast magnetic resonance brain segmentation. IEEE Eng Med Biol Mag. 2001; 20:84–95. [PubMed: 11494774]

Talman JD. Numerical Fourier and Bessel Transforms in Logarithmic Variables. Journal of Computational Physics. 1978; 29:35.10.1016/0021-9991(78)90107-9

Talman JD. NumSBT: A subroutine for calculating spherical Bessel transforms numerically. Computer Physics Communications. 2009; 180:332–338.

Toyoda M, Ozaki T. Fast spherical Bessel transform via fast Fourier transform and recurrence formula. Computer Physics Communications. 2010; 181:277–282.

Wels M, Zheng Y, Huber M, Hornegger J, Comaniciu D. A discriminative model-constrained EM approach to 3D MRI brain tissue classification and intensity non-uniformity correction. Phys Med Biol. 2011; 56:3269–3300. [PubMed: 21558592]

Zavaljevski A, Dhawan AP, Gaskil M, Ball W, Johnson JD. Multi-level adaptive segmentation of multi-parameter MR brain images. Comput Med Imaging Graph. 2000; 24:87–98. [PubMed: 10767588]

Zelditch, M.; Swiderski, D.; Sheets, H.; Fink, W. Geometric Morphometrics for Biologists: A Primer. Elsevier Science. 2004. URL: http://books.google.com/books?id=VJiuHQXlMb4C

Highlights

- A novel spherical wave decomposition (SWD) method is developed.
- SWD allows characterization and automatic segmentation of complex shapes.
- SWD is significantly faster than the current state-of-the-art surface methods.
- SWD is more accurate than the current state-of-the-art surface methods.
- SWD is appropriate for comparative brain anatomy and clinical studies.

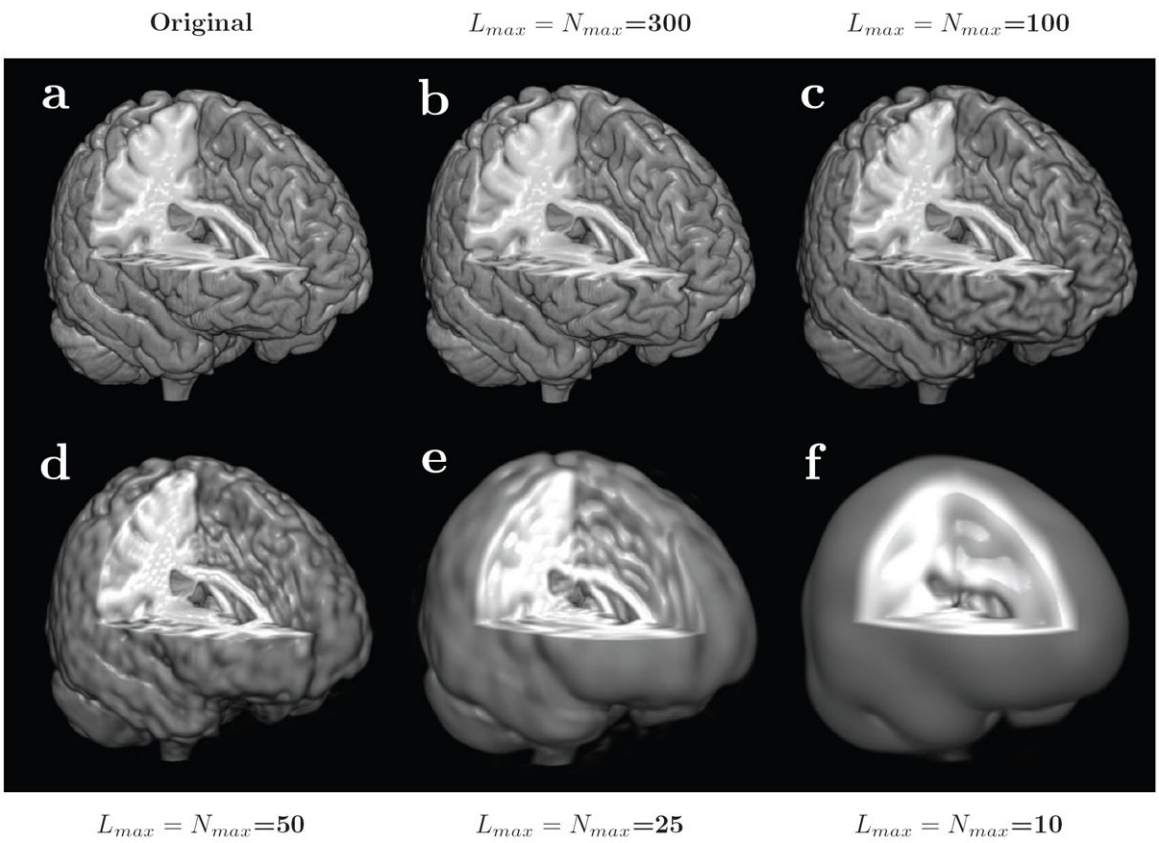

Figure 1.
Series of 3D brain reconstructions obtained with different degrees of SWD (different L_{max} and N_{max} parameters): a) original brain, b)-f) decreasing L_{max} and N_{max} from 300 to 10.

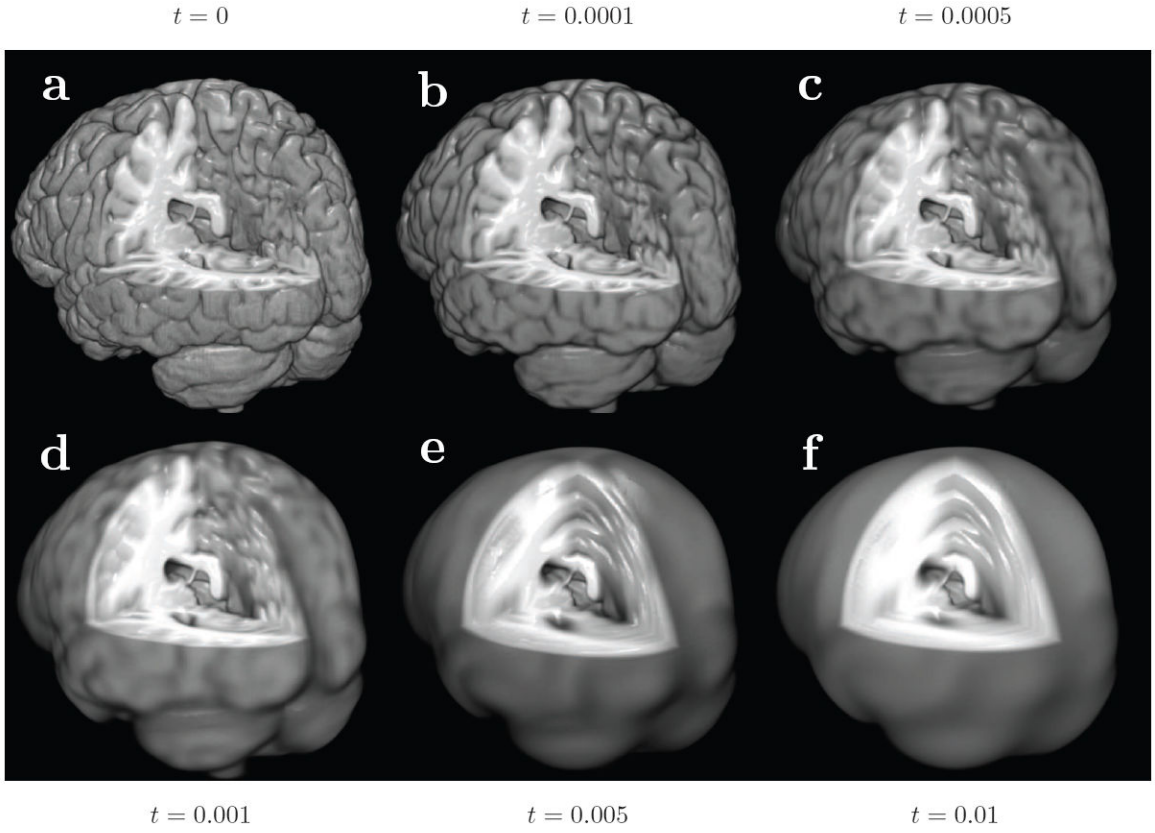

Figure 2.
Weighted Fourier smoothing (WFS) applied to the same 3D brain obtained using SWD with L_{max} = 300, (b-f) for several different values of exponential smoothing factor t from 0.0001 to 0.01, (a) for no smoothing t = 0.

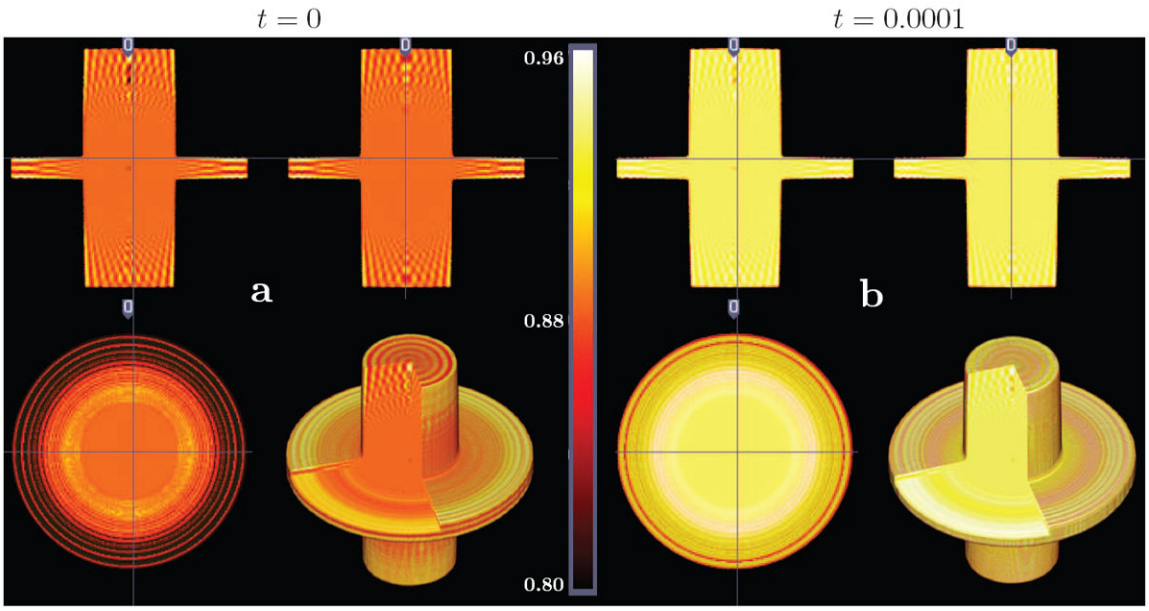

Figure 3.
The SWD representation of a discontinuous (3D step function) shape with $L_{max} = N_{max}$=78 (a) without the WFS (t = 0) and (b) with the WFS (t = 0.0001)

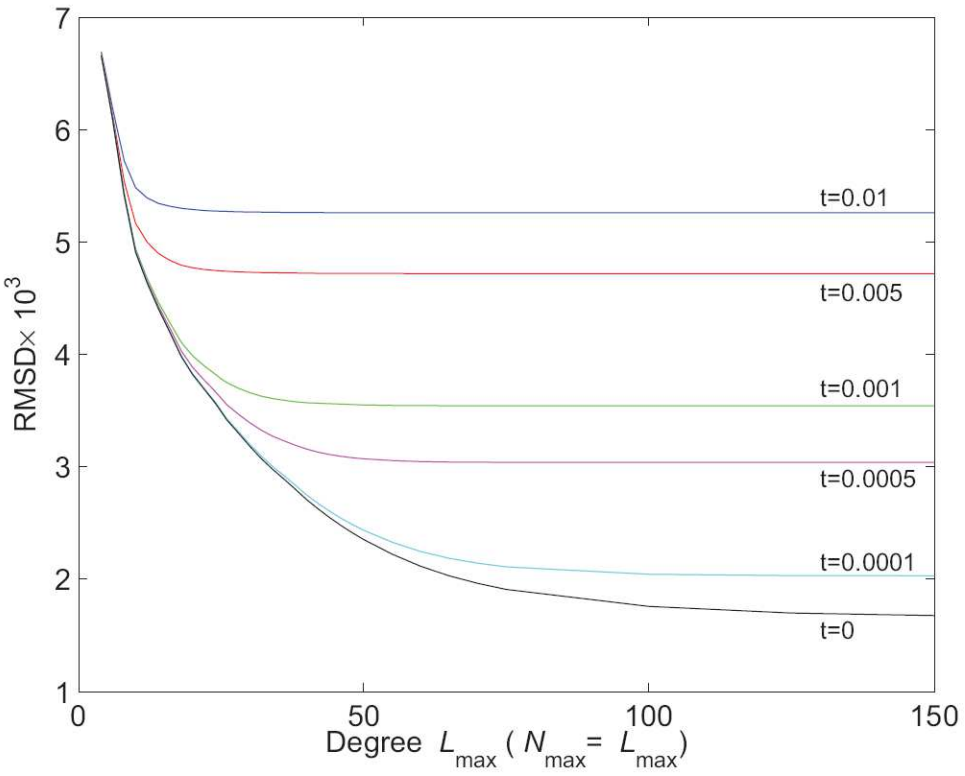

Figure 4.

Plot of root-mean-square-deviation (RMSD) for each of 6 volumes shown in Figure 2 as a function of the SWD degree $L_{max} = N_{max}$. The correspondent exponential smoothing parameters t are printed for each of the RMSD curves.

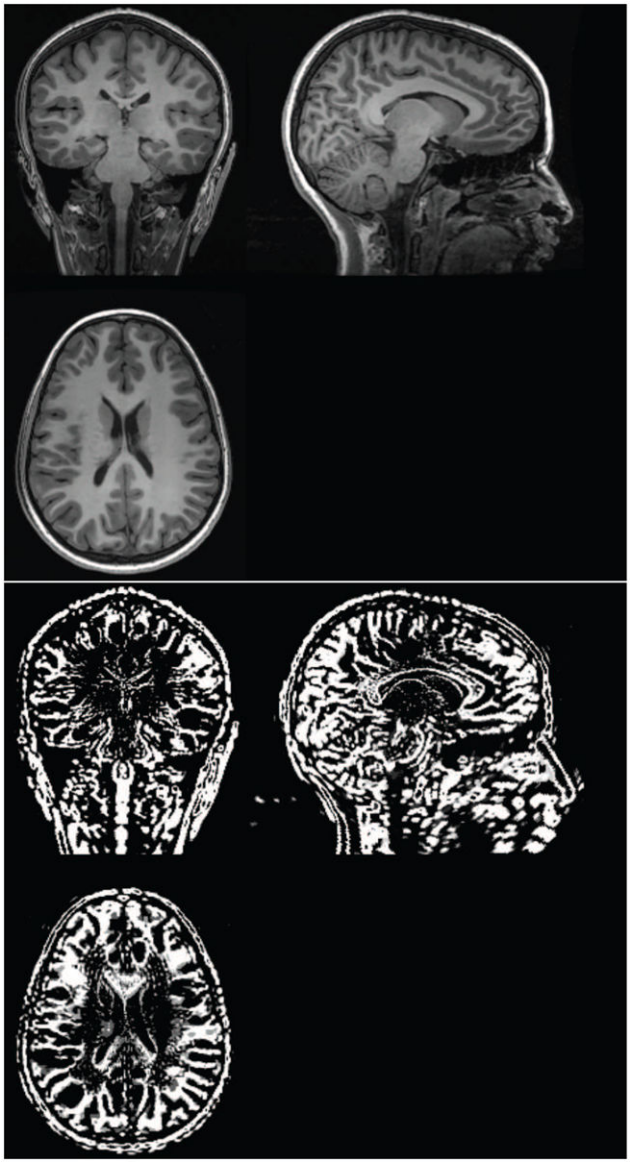

Figure 5.
Anatomical data (top) and derivative (bottom) calculated from the SWD coefficients.

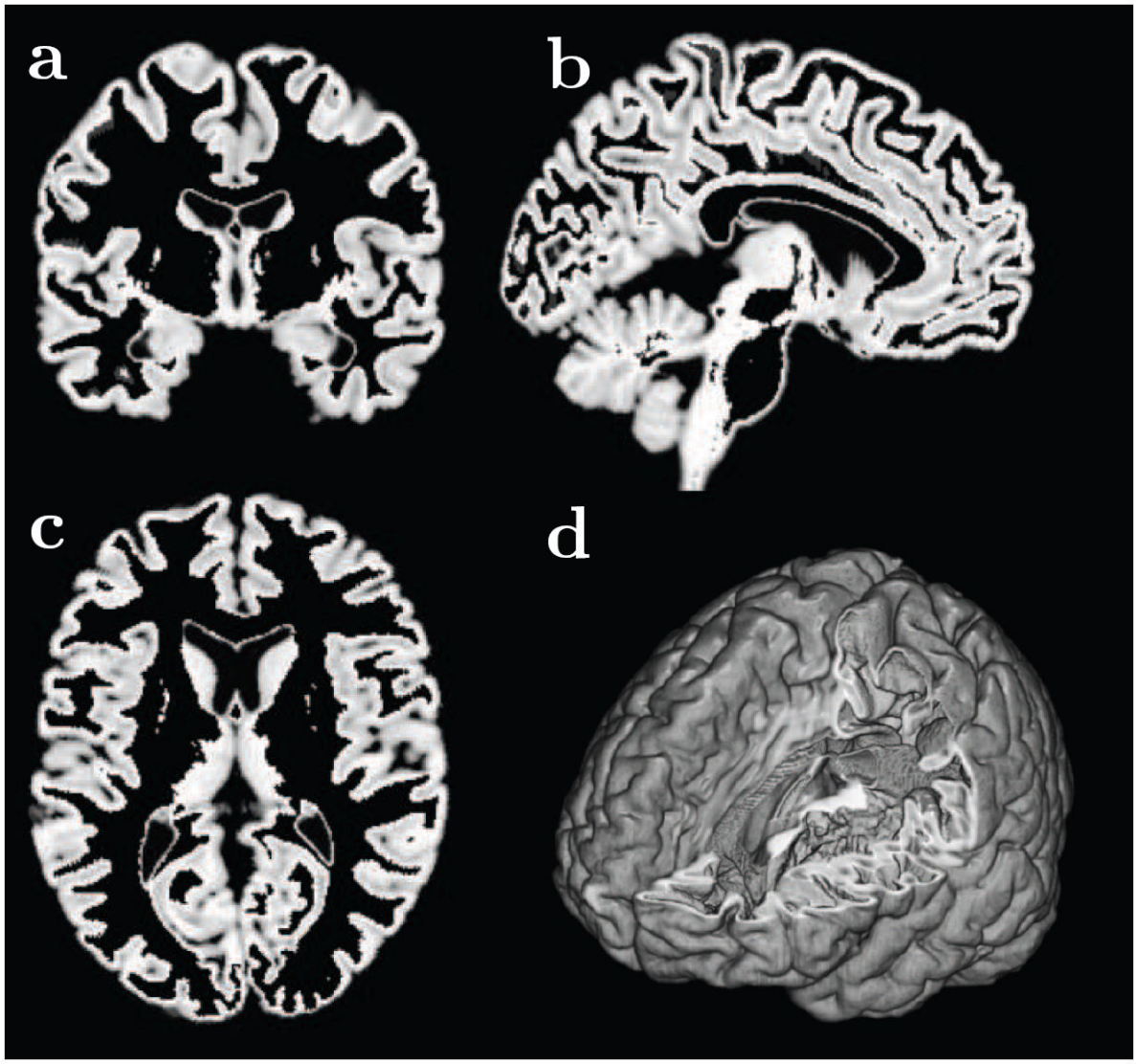

Figure 6.
Gray matter 2D slices (a-c) and 3D view (d) segmented out from the full 3D brain (Figure 1a).

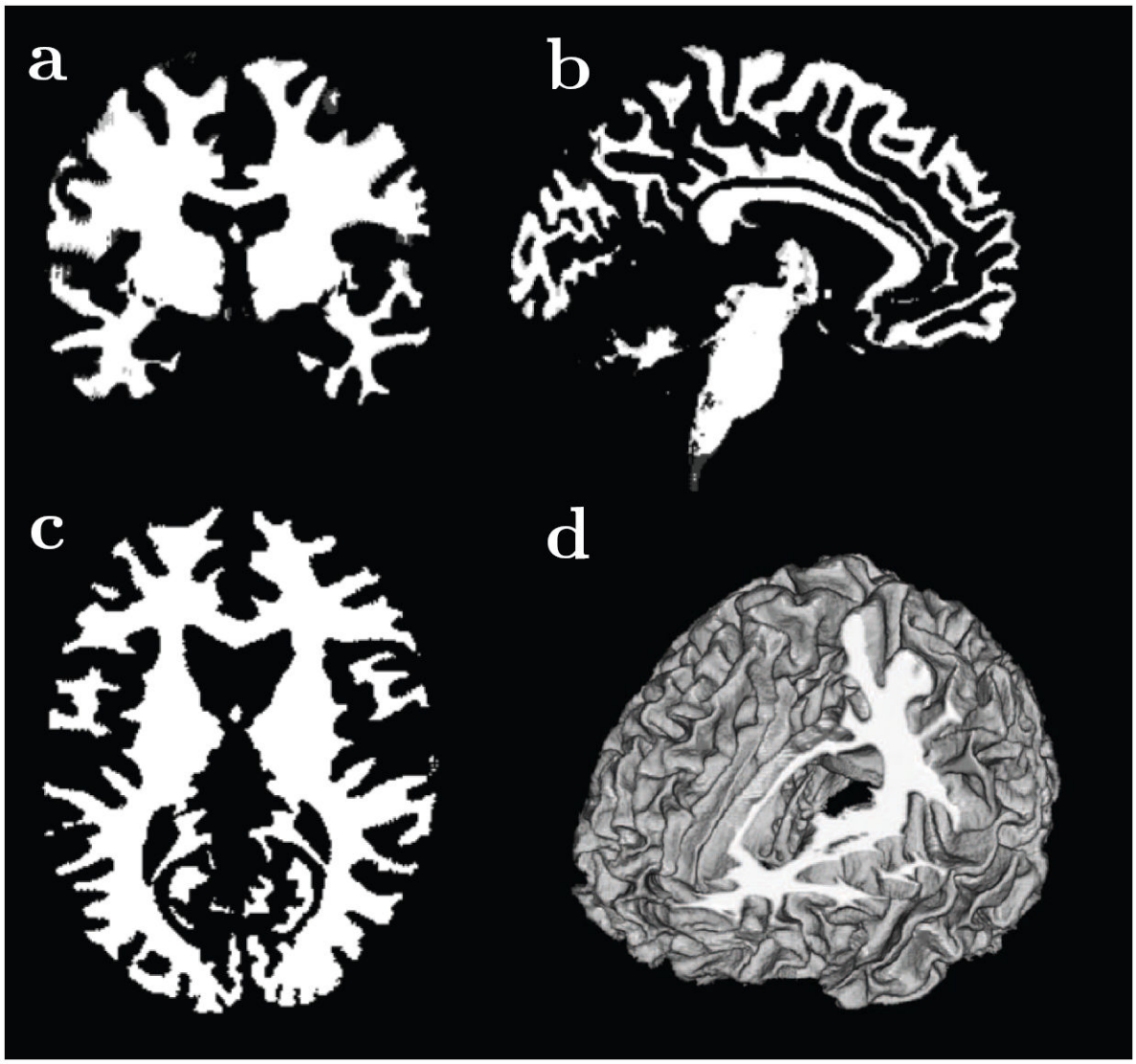

Figure 7.
White matter 2D slices (a-c) and 3D view (d) segmented out from the full 3D brain (Figure 1a)

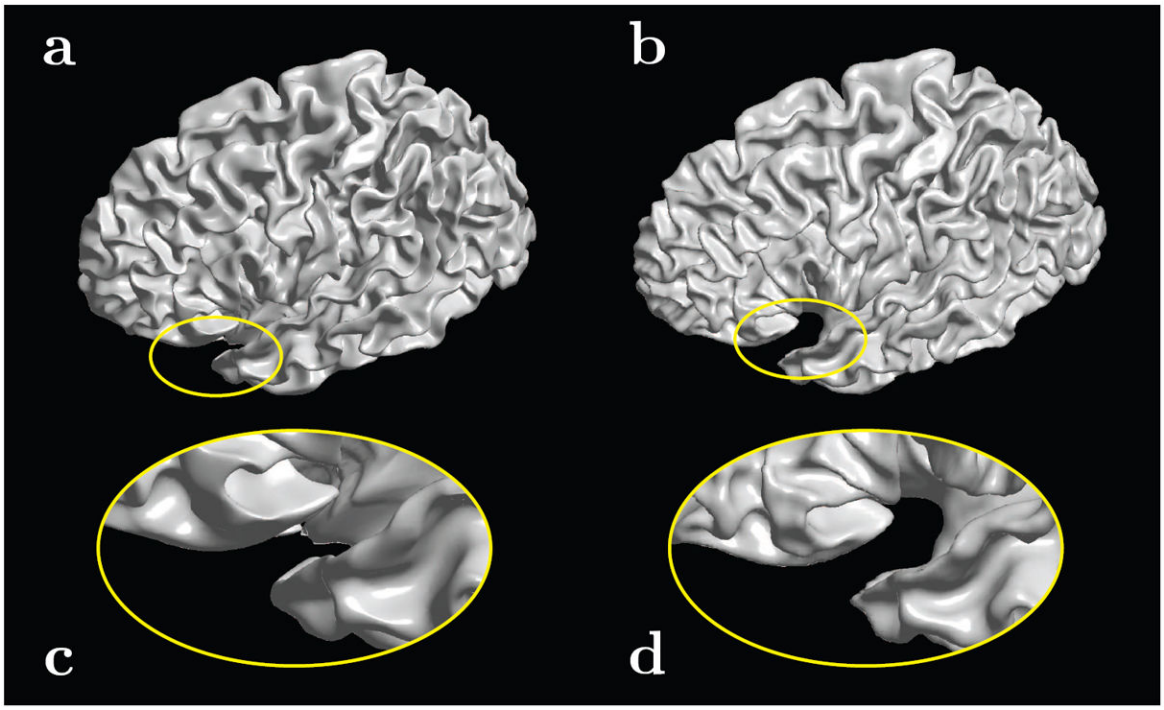

Figure 8.

3D view of white matter left hemisphere obtained from the full 3D brain (Figure 1a) using (a) SPHARM and (b) SWD. The white matter surface used for the SPHARM analysis has been obtained using FreeSurfer (Dale et al., 1999), following all the standard surface extraction steps (segmentation, inflation, fitting, etc.). In addition to 12+ hours total processing time, the SPHARM results clearly show topology related problems (i.e. yellow highlighted bridging, zoomed in panels (c) and (d) for the SPHARM and the SWD respectively). Both SPHARM and SWD results were obtained with 85 degree expansion (due to inability of the SPHARM to process higher degree spherical harmonics).

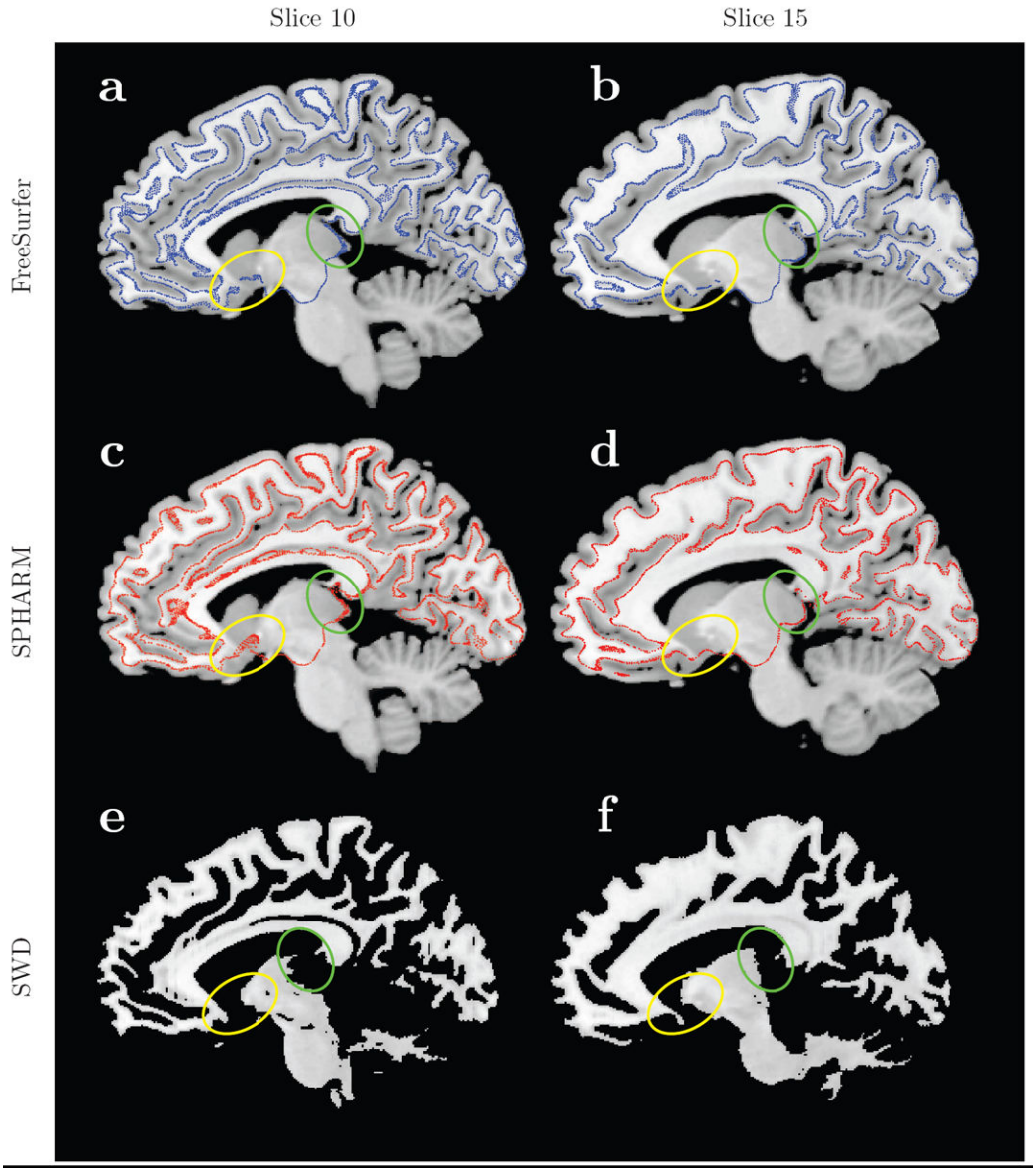

Figure 9.

Two slices of the white matter surface obtained by the FreeSurfer/SPHARM (blue – FreeSurfer, red – SPHARM+FreeSurfer) and overlaid on the gray scale images of the original volumetric data (panels a,b,c and d); and two slices of the white matter volume obtained by the SWD (e and f). Both FreeSurfer and SPHARM slices show incorrect topological bridging in two areas that accented by yellow and green ellipses.

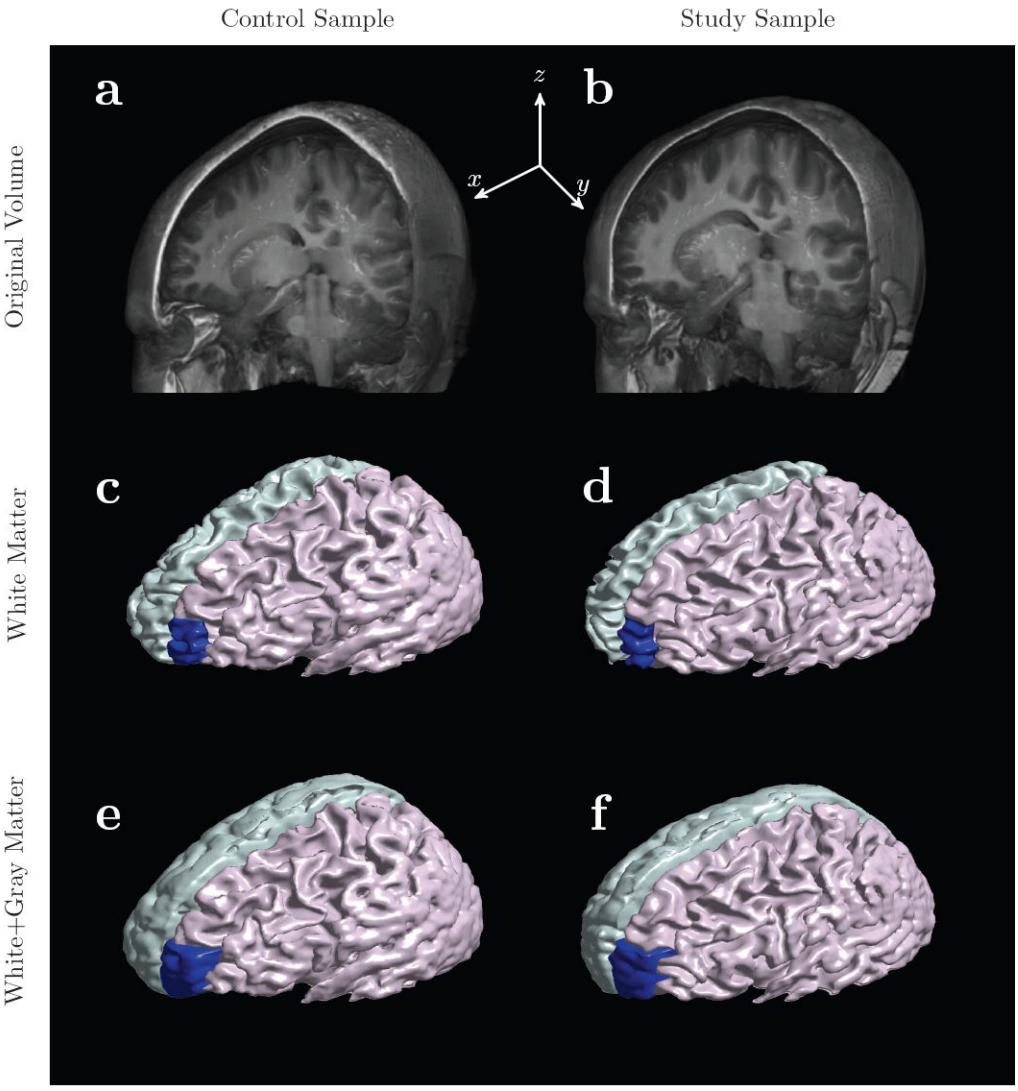

Figure 10.

Various processing stages of two subjects used for cortical thickness measurements in left frontal pole region, that include (1) original anatomical scans (panels a and b), (2) high resolution ($L_{max} = N_{max} = 300$) segmented white matter volume (panels c and d) with the left frontal pole shown in blue, (3) gray matter volumetric layer (panel e and f) shown in its entirety in gray on the right hemisphere, and for the left frontal pole (in blue) on the left hemisphere. The average cortical thickness in the left frontal pole region of the control sample is 2.80mm vs 3.52mm for the study sample.

Table 1

Timing of different stages of SWD method for various degrees of the transform: interpolation to spherical coordinates ($\boldsymbol{F}_x : \mathbf{x} \Rightarrow \mathbf{r}$), forward transform to frequency domain ($f(\mathbf{r}) \Rightarrow f_{lmn}$), backward transform to spherical domain ($f_{lmn} \Rightarrow f(\mathbf{r})$), and interpolation to Cartesian coordinates ($\boldsymbol{F}_r : \mathbf{r} \Rightarrow \mathbf{x}$). All results are for single thread Intel® Core ™ i7-2760QM CPU 2.40GHz.

Order L_{max}	Timings (sec)			
	$\boldsymbol{F}_x : \mathbf{x} \Rightarrow \mathbf{r}$	$f(\mathbf{r}) \Rightarrow f_{lmn}$	$f_{lmn} \Rightarrow f(\mathbf{r})$	$\boldsymbol{F}_r : \mathbf{r} \Rightarrow \mathbf{x}$
400	338.8	56.26	51.95	2.65
300	143.6	20.01	19.22	2.42
200	43.97	4.68	4.99	2.17
100	5.53	0.45	0.46	1.82
50	0.71	0.05	0.05	1.61

Table 2

Timing of different processing steps involved in the SPHARM analysis work-flow vs the overall processing time of the SWD method. All results are for single thread Intel® Core ™ i7-2760QM CPU 2.40GHz.

		SPHARM[a]	SWD
Steps	FreeSurfer	12 hours 50 min[b]	
	SPHARMconstruct	420 sec	
	SPHARMsmooth2	1064 sec	
	SPHARMrepresent2	740 sec[c]	
	Total time	~ 14 hours	$\lesssim$ 10 sec[d]

[a] SPHARM only works for L_{max} up to 85, hence in all timings L_{max} = 85 is used

[b] FreeSurfer time is for the left hemisphere only, add 4.5 hours for both

[c] SPHARMsmooth2 step also includes the SPHARMrepresent2 step

[d] SWD total time includes both the expansion and the derivative calculations for L_{max} = 100 (5.34 sec) and the segmentation step for L_{max} = 85 (3.55 sec)